Supplement of "Atmospheric observations reveal Alaskan wetland CH_4 fluxes are up to threefold higher than process-based model estimates"

Hanyu Liu[1], Charles E. Miller[2], Colm Sweeney[3], Kathryn Mckain[3], Jennifer D. Watts[4], Róisín Commane[5,6], Luke D. Schiferl[6], Zhen Zhang[7], Benjamin Poulter[8], Leyang Feng[1], Ao Chen[1], Ziting Huang[1], Dylan C. Gaeta[1], Kristan L. Morgan[1], William S. Daniels[1], Qiulun Li[1], Joe R. Melton[9], Vineet Yadav[2], Deborah Huntzinger[10], Scot M. Miller[1]

[1]Department of Environmental Health and Engineering, Johns Hopkins University, Baltimore, MD, USA
[2]Jet Propulsion Laboratory, California Institute of Technology, Pasadena, CA, USA
[3]National Oceanic and Atmospheric Administration, Global Monitoring Laboratory, Boulder, CO, USA
[4]Woodwell Climate Research Center, Falmouth, MA, USA
[5]Department of Earth and Environmental Sciences, Columbia University, New York, NY, USA
[6]Lamont-Doherty Earth Observatory, Columbia University, Palisades, NY, USA
[7]Institute of Tibetan Plateau Research, Chinese Academy of Sciences, Beijing, China
[8]Spark Climate Solutions, San Francisco, CA, USA
[9]Environment and Climate Change Canada, Victoria, BC, Canada
[10]School of Earth and Sustainability, Northern Arizona University, Flagstaff, AZ, USA

Hanyu Liu et al.
Correspondence to: Hanyu Liu (hliu154@jhu.edu)

Contents of this file

1. Tables S1 to S2
2. Figures S1 to S8

Details on the WETCHIMP models

Model	Spatial Resolution ($lat \times long$)	References
CLM4Me	$2.5° \times 1.9°$	Riley et al., 2011
DLEM	$0.5° \times 0.5°$	Tian et al., 2010a
LPJ-WSL	$0.5° \times 0.5°$	Hodson et al., 2011
LPJ-WhyMe	$0.5° \times 0.5°$	Wania et al., 2010a
LPJ-Bern	$0.5° \times 0.5°$	Spahni et al., 2011
ORCHIDEE	$1.0° \times 1.0°$	Ringeval et al., 2010
SDGVM	$0.5° \times 0.5°$	Singarayer et al., 2011

Table S1. The seven global wetland flux models from WETCHIMP that we use in the study. The original spatial resolution in $lat \times long$ is also shown for each model.

Details on the GCP models

Model	Spatial Resolution ($lat \times long$)	References
$CH_4MOD_{wetland}$	$0.5° \times 0.5°$	Li et al., 2010
CLASSIC	T63 ($\sim 2.8°$)	Arora et al., 2018
DLEM	$0.5° \times 0.5°$	Tian et al., 2010b
ELM-ECA	$\sim 2° \times \sim 2°$	Zhu et al., 2019
ISAM	$0.5° \times 0.5°$	Shu et al., 2020
JSBACH	$1.875° \times 1.875°$	Kleinen et al., 2020
JULES	$0.5° \times 0.5°$	Clark et al., 2011
LPJ-GUESS	$0.5° \times 0.5°$	McGuire et al., 2012; Wania et al., 2010b
LPJ-MPI	$0.5° \times 0.5°$	Kleinen et al., 2012
LPJ-wsl	$0.5° \times 0.5°$	Zhang et al., 2016
LPX-Bern	$0.5° \times 0.5°$	Spahni et al., 2011
ORCHIDEE	$1° \times 1°$	Ringeval et al., 2010
SDGVM	$0.5° \times 0.5°$	Singarayer et al., 2011
TEM-MDM	$0.5° \times 0.5°$	Liu et al., 2020
TRIPLEX-GHG	$0.5° \times 0.5°$	Zhu et al., 2014
VISIT	$0.5° \times 0.5°$	Ito and Inatomi, 2012

Table S2. The 16 GCP global wetland flux models that we use in the study, including the number of global latitude and longitude grid cells in each model. Model names in bold indicate models for which both diagnostic and prognostic simulations are available.

Additional sensitivity matrices

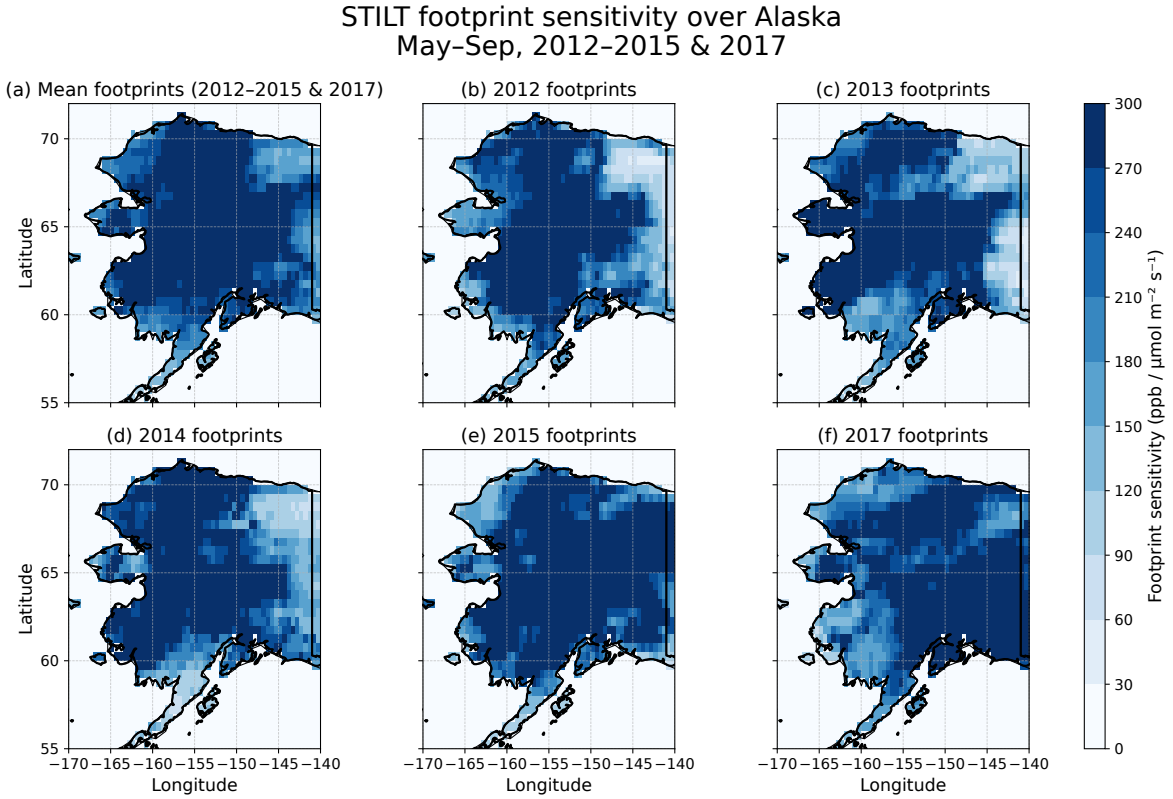


Figure S1. The mean WRF-STILT footprints in Alaska using growing season (May to September) atmospheric observations from CARVE and Arctic-CAP. Each panel represents (a) five years mean, (b) 2012, (c) 2013, (d) 2014, (e) 2015, and (f) 2017.

Atmospheric comparisons

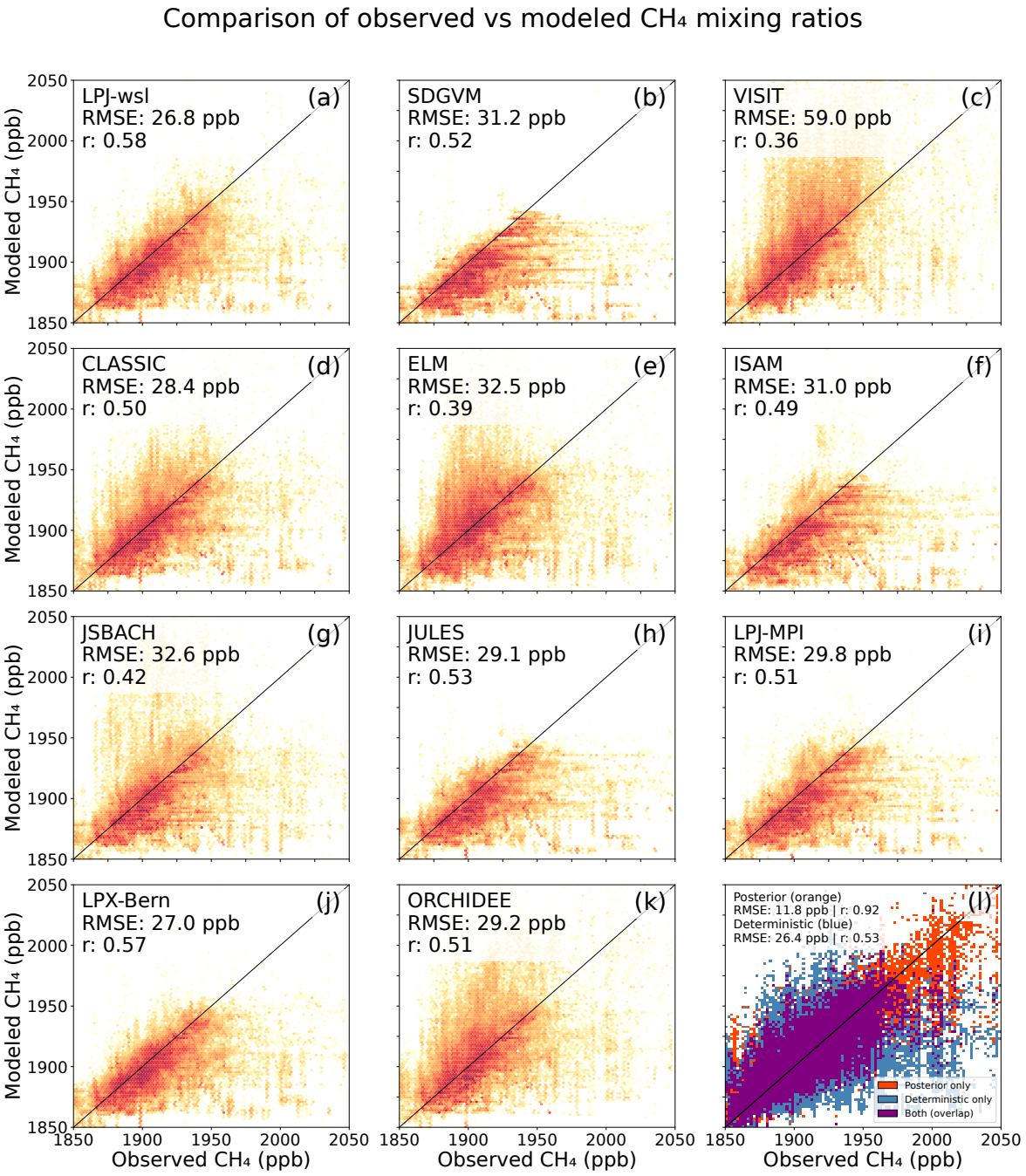


Figure S2. Correlation coefficient comparisons using WRF-STILT modeled CH_4 mixing ratios from the prognostic GCP models and from our posterior and deterministic estimates against aircraft observations from CARVE and Arctic-CAP. Darker red dots indicate higher point density, and the black line denotes the 1:1 line for reference. The purple dots in sub-plot (l) represent the data points for both posterior and deterministic estimates, whereas the orange dots represent the posterior estimates only and blue dots represent deterministic estimates only.

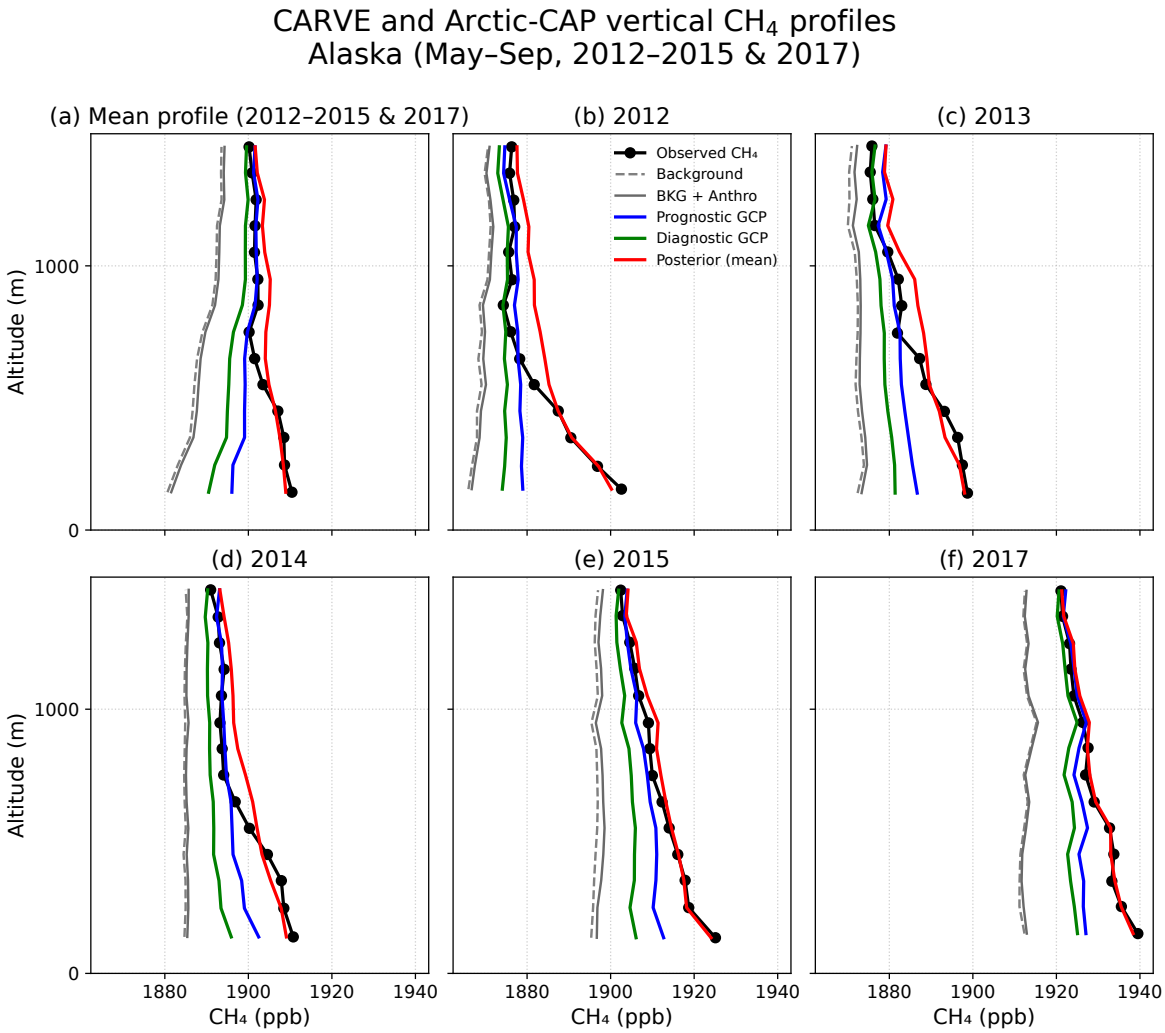


Figure S3. The comparisons of the vertical profiles between WRF-STILT modeled CH_4 mixing ratios from the prognostic and diagnostic GCP models and from our posterior estimates against aircraft observations from CARVE and Arctic-CAP. Panel (a) represents the mean vertical profile comparisons across all years, (b) to (f) represent the mean vertical profile comparisons across individual years. The blue lines denote the total modeled mixing ratios using prognostic GCP models, the green lines show the total modeled mixing ratios using diagnostic GCP models, the dashed gray lines exhibit the background values derived from the mean of atmospheric observations collected over 2000 meters above ground level, and the solid gray lines represent the sum between the background values and the modeled mixing ratios from all other non-wetland sector fluxes. The unit is in ppb and the observations that we use in this study are all below 1500 meters above ground level.

Inundation fraction maps

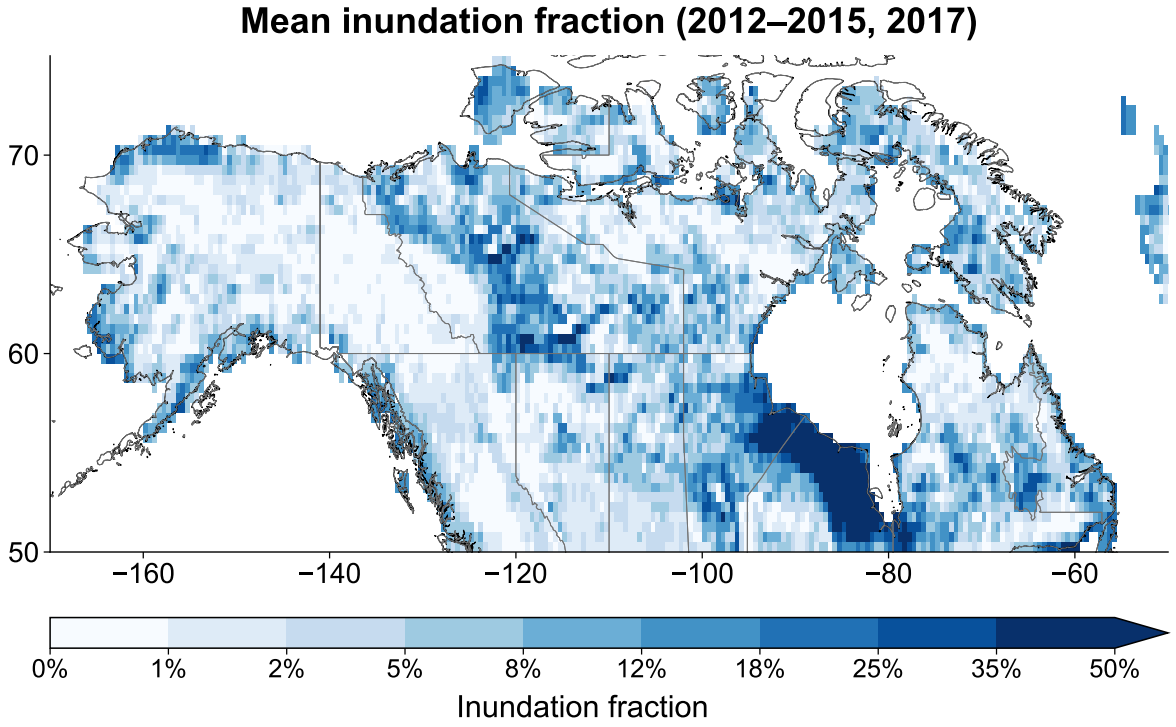


Figure S4. Mean inundation fraction (wetland extent) for the growing seasons (May–September) of 2012–2015 and 2017, based on the WAD2M v2 product and regridded to a 0.5°× 0.5° spatial resolution. Values represent the grid-cell fraction that is inundated (unitless, with 0.2 corresponding to 20% inundation). The map covers Alaska and adjacent regions of Canada within the WRF–STILT modeling domain used in this study.

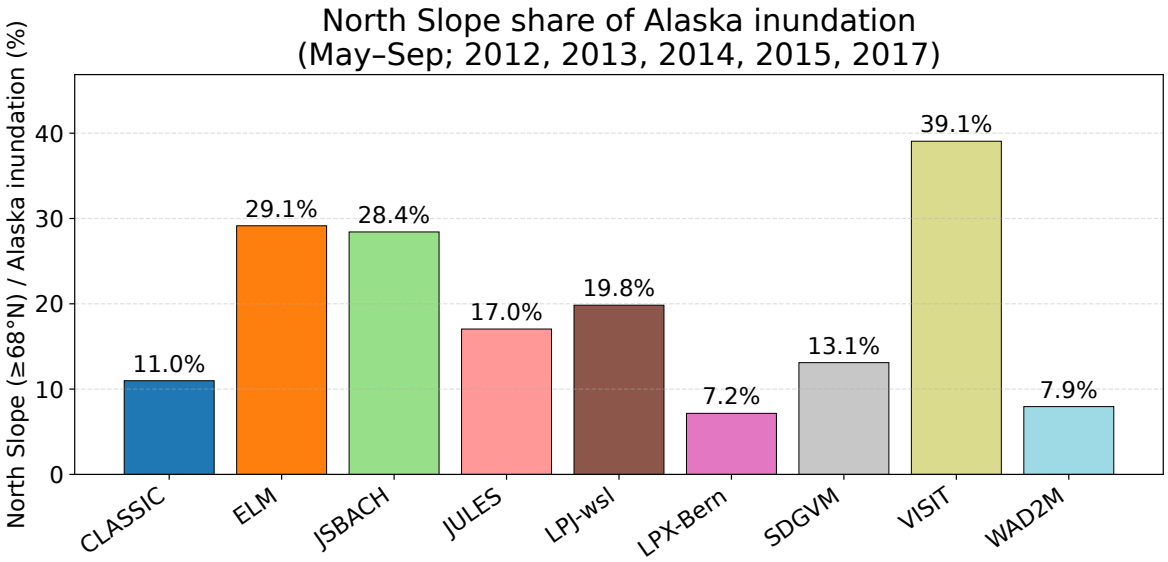


Figure S5. North Slope ($\geq$ 68°N) share of Alaska's total inundated area for eight prognostic GCP models and the WAD2M v2 product. For each model and year (2012, 2013, 2014, 2015, 2017), we first compute the May–September mean inundation fraction (Fw) at each land grid cell. We then calculate the total inundated area in the North Slope and in all of Alaska, and express the North Slope share as the ratio of these two totals (in %). For each model, the bar shows the mean North Slope share within a year and then averaged across years. The WAD2M v2 bar represents the same metric computed from the WAD2M wetland extent product used by all diagnostic GCP models.

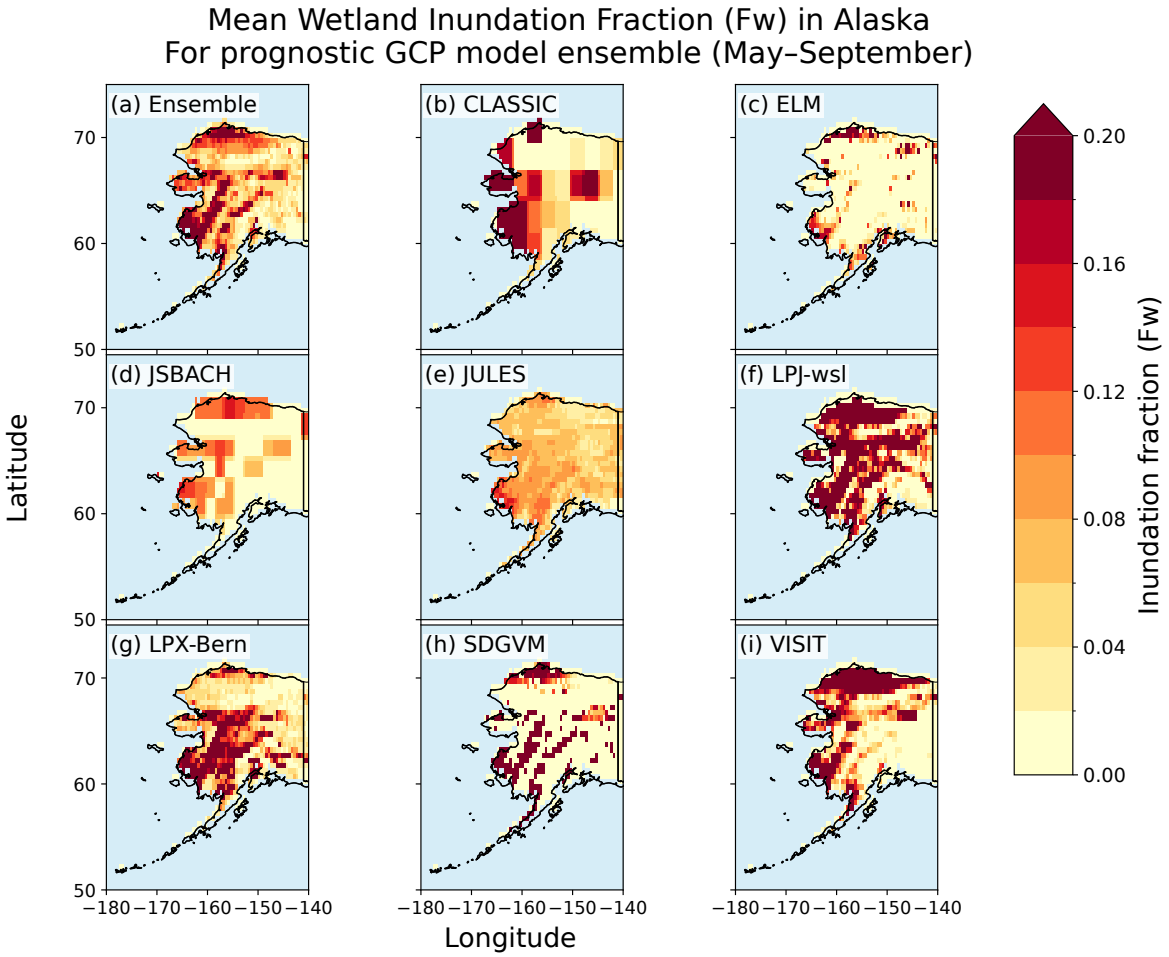


Figure S6. The mean Alaskan inundation fraction maps from May to September (2012 to 2015, and 2017) for (a) ensemble of all available prognostic inundation fraction maps, and (b) to (i) showing individual inundation fraction maps from these prognostic GCP models. The unit is in %, and a 0.2 means that 20% of the areas within a grid box is inundated.

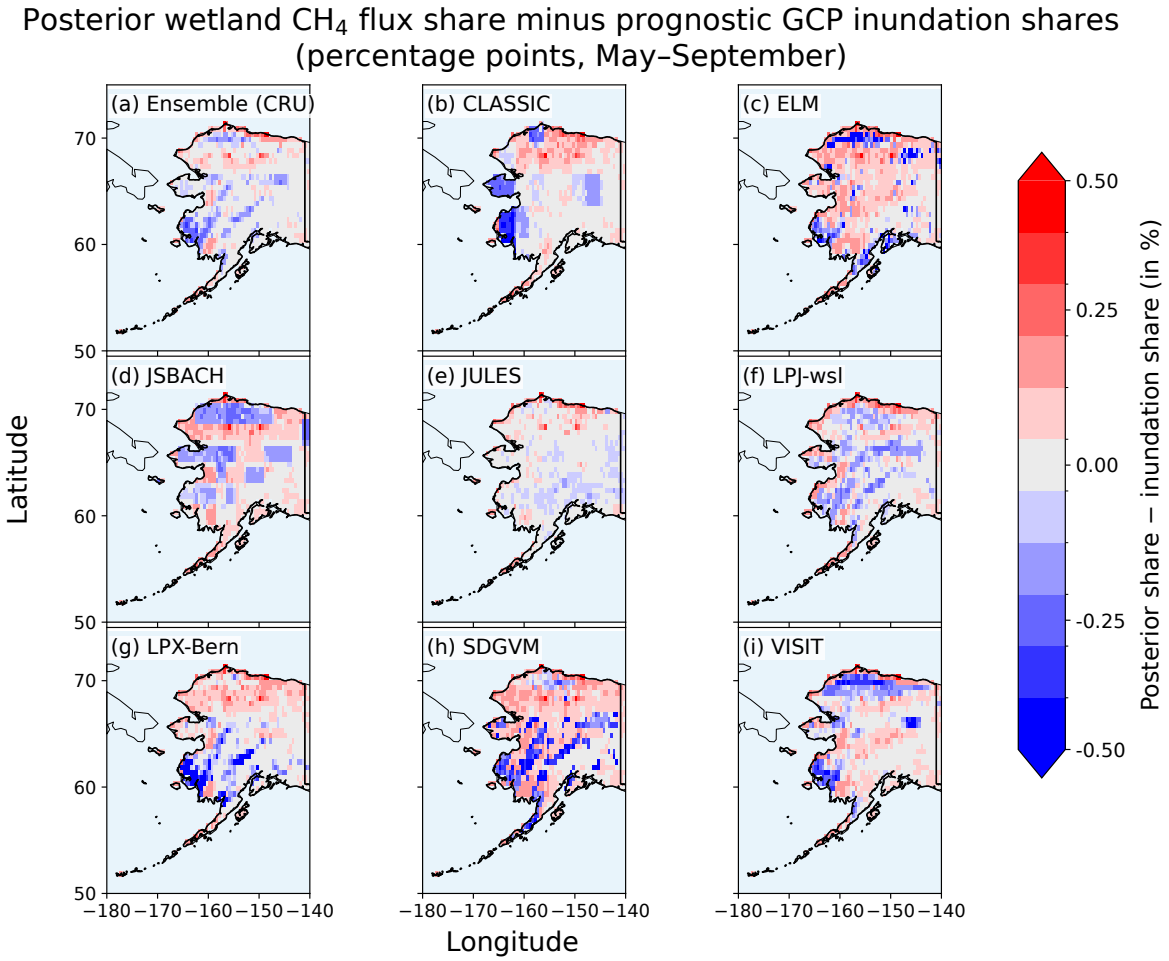


Figure S7. Difference between the spatial distribution of posterior CH_4 flux shares and prognostic inundation shares (percentage points) at 0.5° resolution. For each grid cell, we compute its percentage contribution to the total Alaskan CH_4 flux using the posterior flux estimates and its percentage contribution to the total Alaskan inundated area using the wetland extent products. The common color scale spans −0.50 to +0.50 percentage points for all panels. Panel (a) shows the difference between posterior flux shares and the ensemble-mean inundation shares across all prognostic GCP models, while panels (b)–(i) show the corresponding differences for individual prognostic GCP models. Red regions indicate grid cells where posterior flux estimates assign a larger fraction of Alaska's total CH_4 flux than implied by the model inundation (posterior > inundation), suggesting that wetlands may be underrepresented in the extent product. Blue regions indicate grid cells where the inundation products give more shares than the posterior flux estimates (posterior < inundation), suggesting possible overrepresented wetlands. Cells with small absolute differences ($|\Delta| < 0.05$ percentage points) appear in light gray, and ocean grid cells and land east of 140°W are masked.

Additional details on IAV

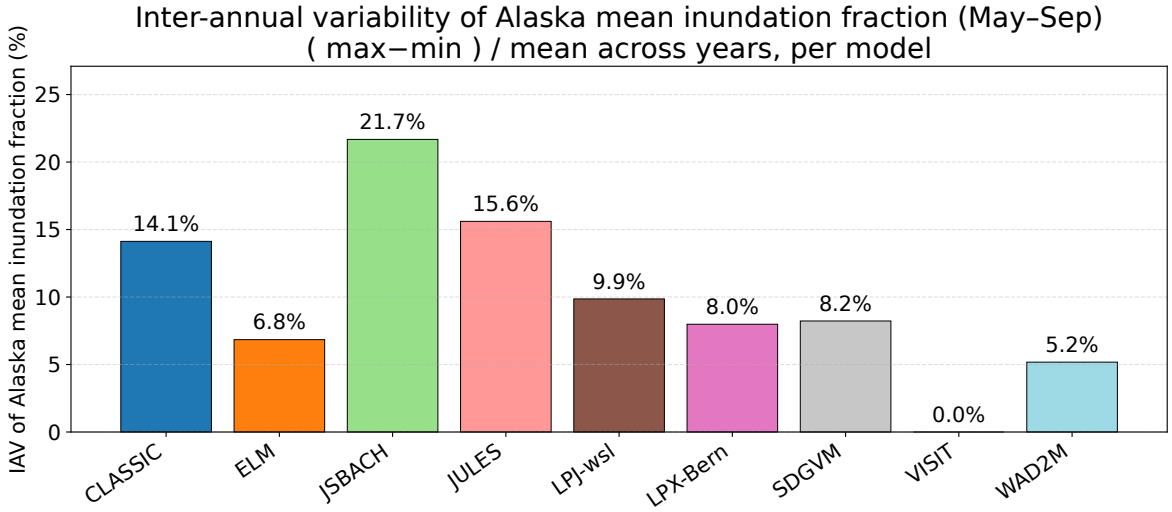


Figure S8. Inter-annual variability of Alaska-mean inundation fractions simulated by the prognostic GCP models and by the WAD2M v2 product for the growing seasons (May–September) of 2012, 2013, 2014, 2015, and 2017. For each model and each year, we calculate the Alaskan mean inundation fraction by averaging monthly values over the growing season and multiply by grid-cell area. The inter-annual variability for each model is expressed as the difference between its highest and lowest Alaska-mean inundation values across the five study years, divided by the multi-year average of those values (in %). A higher IAV indicates that the model's inundated areas change more quickly from year to year.

North Slope share: inundation vs CH_4 flux

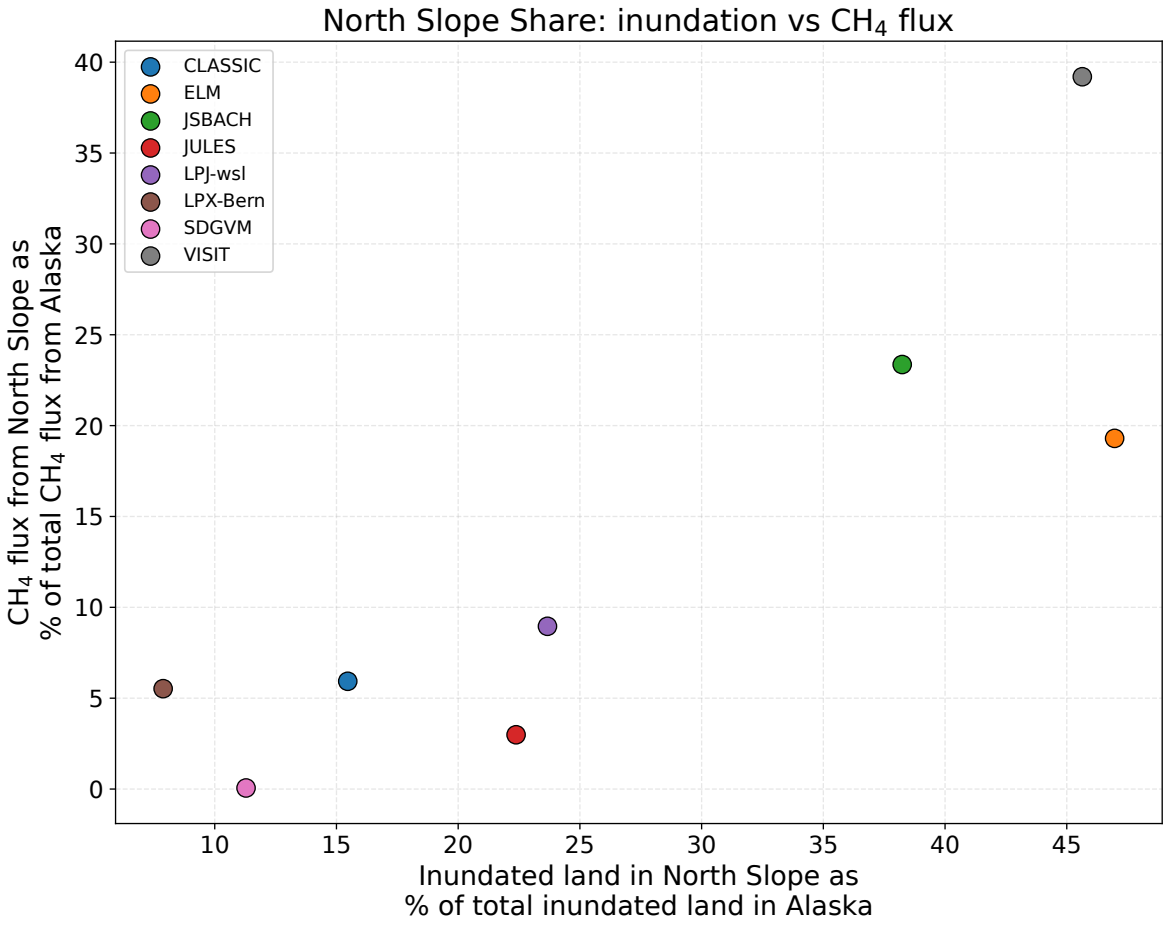


Figure S9. The comparison of North Slope shares of statewide inundation and CH_4 fluxes across prognostic GCP models. Each colored dot represents a prognostic GCP model, with the x-axis showing the percentage of total Alaskan inundated areas from the North Slope and the y-axis showing the percentage of total Alaskan CH_4 flux from the North Slope. Model values are averaged across the May–September period for years from 2012–2015 and 2017.

IAV: inundation vs CH_4 flux

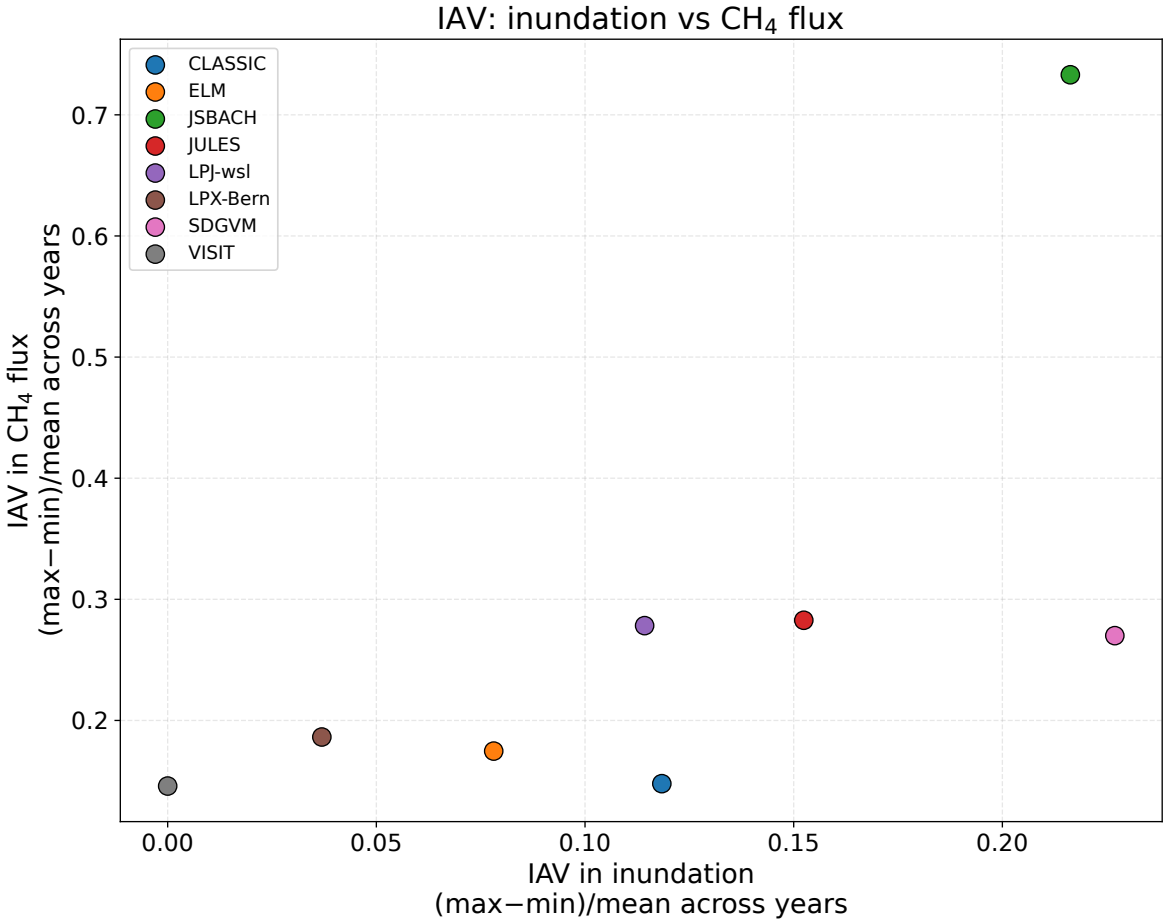


Figure S10. Comparison of IAV in inundation and CH_4 fluxes across prognostic GCP models. Each marker represents a prognostic GCP model. The x-axis represents IAV of total Alaskan inundation and the y-axis represents the IAV of total Alaskan CH_4 fluxes across 2012 to 2015, and 2017 from May to September.

Mean fall-shoulder season posterior CH_4 flux estimate

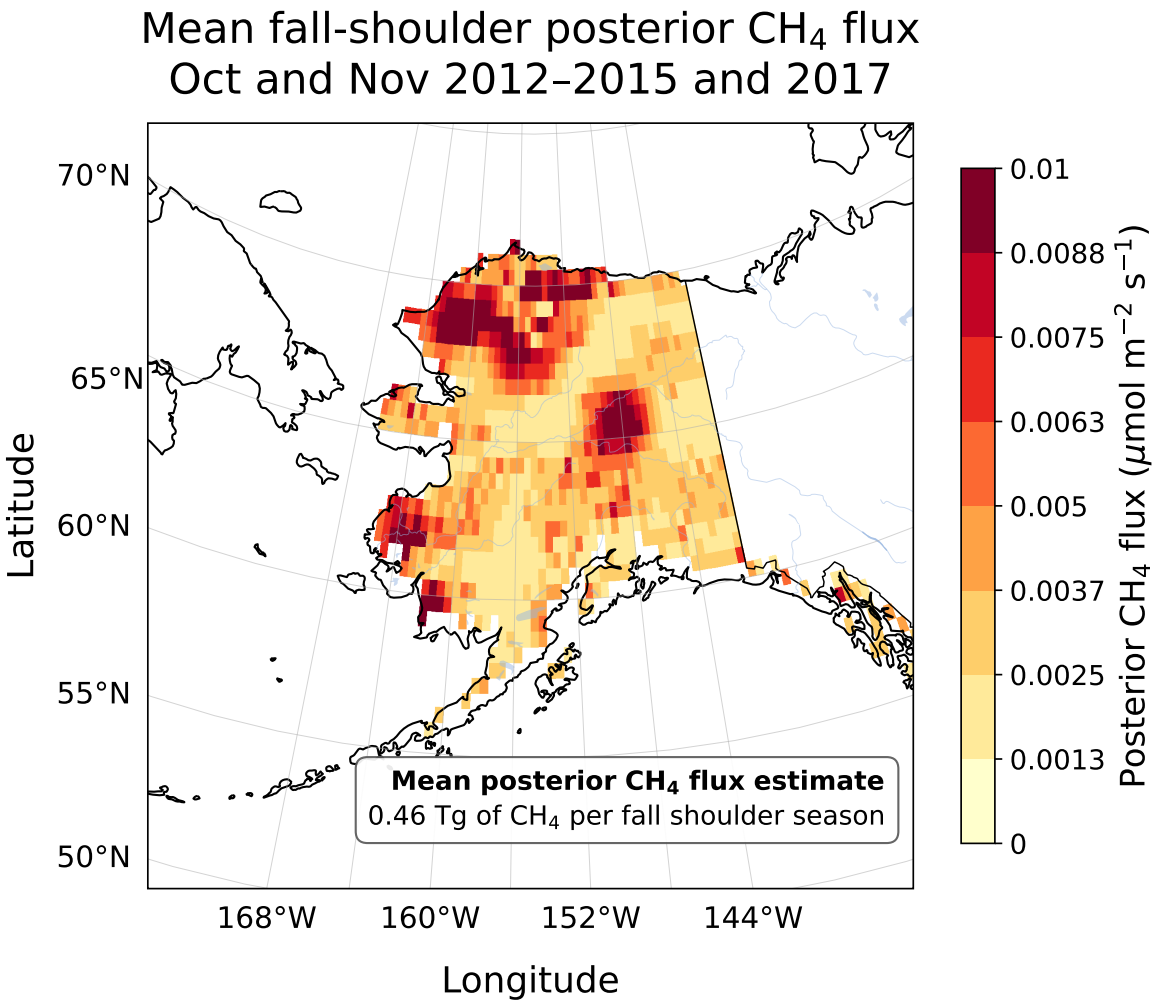


Figure S11. The spatial distribution of mean fall-shoulder season (October and November) posterior CH_4 flux estimate from 2012 to 2015, and 2017. All grid-cell values are expressed in units of μmol m^{-2} s^{-1}.

Posterior and GCP model CH_4 flux distributions across Alaskan permafrost zones

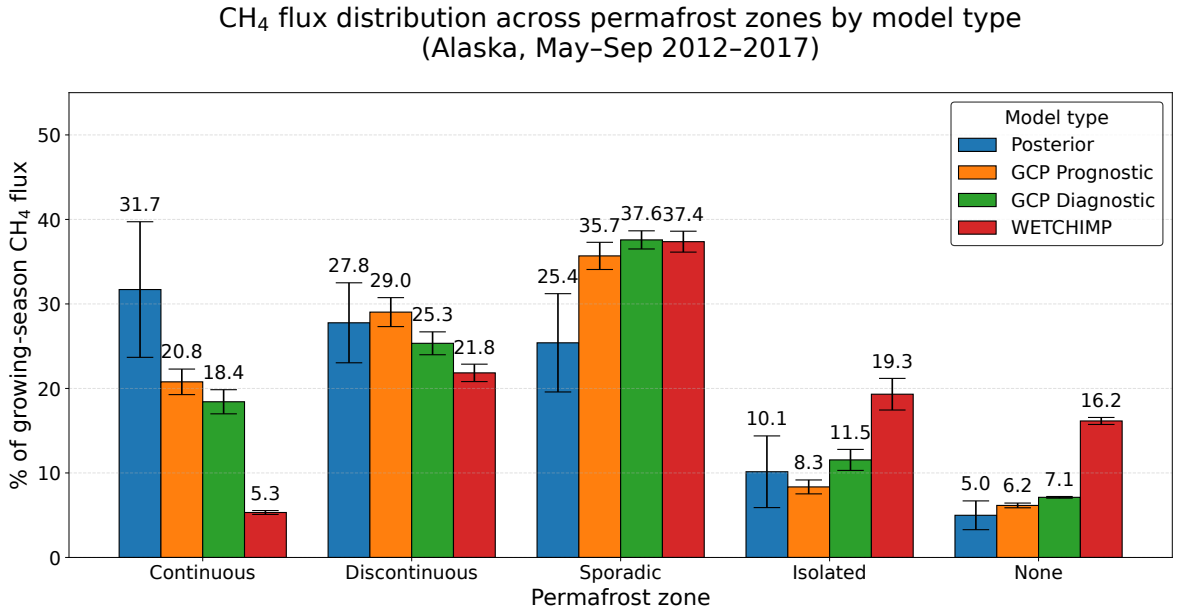


Figure S12. The percentage of growing-season (May–Sep) CH_4 flux by permafrost zone based on the permafrost extent product from the European Space Agency's (ESA) Climate Change Initiative (CCI) Permafrost project (Westermann et al., 2024). The permafrost extent product groups grid cells into continuous (≥90 %), discontinuous (50-90 %), sporadic (10–50 %), isolated (0–10 %), and none (0 %) permafrost zones. These colored bars are denoted as the posterior estimate (blue), GCP prognostic (orange), and GCP diagnostic (green) wetland ensembles over Alaska. Bars show the mean percentage of CH_4 fluxes over different permafrost zones in Alaska across the 2012–2015 and 2017 study year. For each year, we first calculated the ensemble mean across all GCP models. We then calculated the interannual standard deviation from these annual ensemble means. The error bars indicate ±1 interannual standard deviation across each model (or model ensemble) type for the same study years in Alaska.

Spatial distribution of posterior and GCP model CH_4 flux estimates across Alaskan permafrost zones

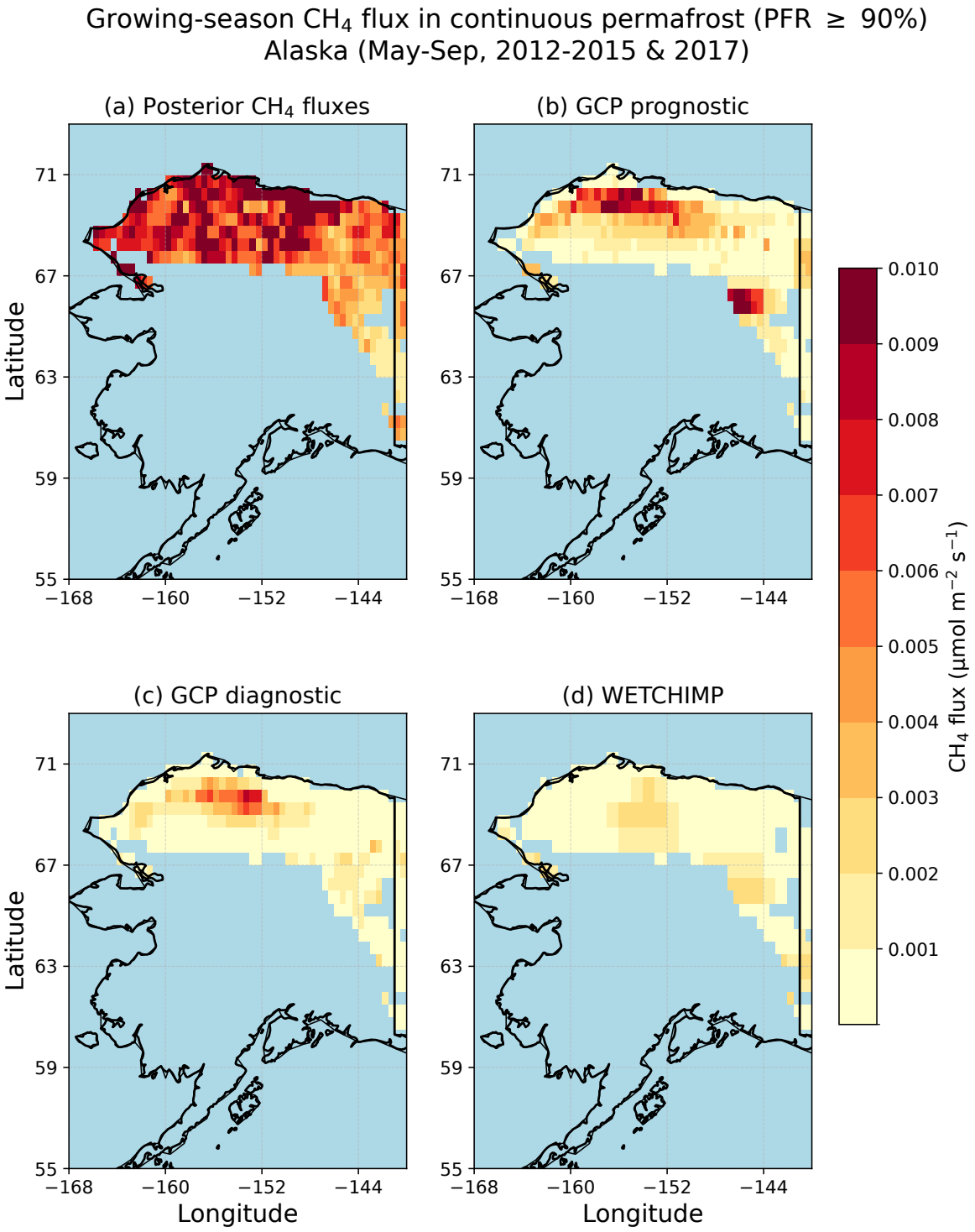


Figure S13. The spatial differences of estimated CH_4 fluxes between posterior estimate and process-based model ensembles during the growing-seasons in 2012 to 2015, and 2017 in Alaska's continuous permafrost region. Panel (a) represents the posterior flux estimate. Panel (b) represents GCP model ensemble mean with prognostic runs. Panel (c) represents GCP model ensemble mean with diagnostic runs. Panel (d) demonstrates the WETCHIMP model ensemble mean. All grid-cell values are expressed in units of μmol m^{-2} s^{-1}, and the spatial domain is 55°N to 72°N and 170°W to 140°W.

S0.1 Additional details on the GIM

To determine the best estimate of the fluxes, we minimize a cost function that balances how well the estimate matches our atmospheric CH_4 observations ($\boldsymbol{z}$) against how closely the estimate matches the predicted fluxes generated by our environmental drivers ($\mathbf{X}\boldsymbol{\beta}$). The standard equation of the cost function can be expressed as (e.g., Kitanidis & Vomvoris, 1983; Michalak et al., 2004):

$$\mathcal{L}_{s,\beta} = \tfrac{1}{2}(\boldsymbol{z} - \mathbf{H}\boldsymbol{s})^T \mathbf{R}^{-1}(\boldsymbol{z} - \mathbf{H}\boldsymbol{s}) + \tfrac{1}{2}(\boldsymbol{s} - \mathbf{X}\boldsymbol{\beta})^T \mathbf{Q}^{-1}(\boldsymbol{s} - \mathbf{X}\boldsymbol{\beta}). \tag{S1}$$

Here, the first term on the right-hand side of Eq. (S1) governs how strongly the inverse model fits the atmospheric measurements by penalizing mismatches between the observed ($\boldsymbol{z}$) and modeled mixing ratios ($\mathbf{H}\boldsymbol{s}$), weighted by $\mathbf{R}$. $\mathbf{R}$ is the model-data mismatch covariance matrix with dimensions $n \times n$, where n represents the number of atmospheric CH_4 observations. The model-data mismatch includes errors that are not fully explained by the estimated fluxes, such as measurement errors and atmospheric transport errors. In our implementation, the diagonal elements of $\mathbf{R}$ are the variances of the model-data mismatch errors for individual atmospheric observations. In our setup, we set the off-diagonal values of $\mathbf{R}$ to zero, meaning that model-data mismatch errors are assumed to be independent across observations. A smaller diagonal value in $\mathbf{R}$ means that our inverse model trusts the observations more and that the posterior flux estimate ($\boldsymbol{s}$) is more strongly adjusted to reduce the discrepancy between modeled and observed CH_4 mixing ratios.

On the other hand, the second term on the right-hand side of Eq. (S1) penalizes the difference between the true and unknown flux estimate ($\boldsymbol{s}$) from the deterministic model ($\mathbf{X}\boldsymbol{\beta}$), weighted by $\mathbf{Q}$. $\mathbf{Q}$ is the covariance matrix of the stochastic component ($\boldsymbol{\xi}$) with dimensions $m \times m$, where m represents the total number of grid boxes across space and time. As mentioned in the main article, the stochastic component helps adjust the spatiotemporal patterns of the flux estimate that are not explained by the deterministic component ($\mathbf{X}\boldsymbol{\beta}$). The adjustments to the fluxes made by the stochastic component will better match the flux estimate with the atmospheric CH_4 observations from CARVE and Arctic-CAP. Here, $\mathbf{X}$ is an $m \times p$ matrix ($m = 634{,}338$, $p = 2$) containing the environmental driver data. The first column of $\mathbf{X}$ is a constant column of ones that plays a role similar to the intercept term in a regression. Existing geostatistical modeling studies commonly include this column of ones, and we do so here as well (e.g., Gourdji et al., 2012; Miller, Worthy, et al., 2014; Miller et al., 2016). In this setup, we also interact or multiply the environmental drivers with one another, as was done in Miller, Worthy, et al. (2014) and Miller et al. (2016), and the product of these variables becomes the second column of $\mathbf{X}$. We interact or multiply these environmental driver variables because the effect of one variable often depends on the value of another. For example, inundated soils produce more methane when temperatures are warmer, so the effect of inundation likely interacts with the effect of temperature. In addition, $\boldsymbol{\beta}$ (dimensions of $p \times 1$) is a vector of coefficients, and our inverse model will estimate $\boldsymbol{\beta}$ to scale the estimates from the deterministic component and produce the best match against atmospheric observations. Furthermore, $\mathbf{Q}$ controls how strongly the true flux estimate is constrained by the deterministic component ($\mathbf{X}\boldsymbol{\beta}$). In this case, the diagonal elements of $\mathbf{Q}$ represent the variance of the fluxes that are not captured by the deterministic component (i.e., the stochastic component), while the off-diagonal elements describe the spatial and temporal correlation structure of the stochastic component $\boldsymbol{\xi}$.

Before running the inverse model, we first need to estimate the covariance parameters that define $\mathbf{R}$ and $\mathbf{Q}$. In our case, we use a approach called the restricted maximum likelihood (RML), which is widely used by numerous existing studies (e.g., Kitanidis & Lane, 1985; Michalak et al., 2004; Miller, Worthy, et al., 2014; Miller et al., 2016). RML is a statistical approach that will estimate the covariance parameters that are statistically most likely given the spatial and temporal patterns in the atmospheric CH_4 observations. Using this approach, we estimate a value of $(10.92\text{ppb})^2$ for the diagonal elements of $\mathbf{R}$. We estimate a value of $(0.05\ \mu\text{mol}\,CH_4\,m^{-2}\,s^{-1})^2$ for the diagonal elements of $\mathbf{Q}$, a value of 105 days for the correlation time, and a value of 187 km for the correlation length. More details on RML and covariance parameter estimation are explained in Michalak et al. (2004).

To minimize the cost function, we first solve a system of linear equations to estimate $\boldsymbol{\beta}$ and $\boldsymbol{s}$ (**Kitanidis1996b**; Michalak et al., 2004). To solve for $\boldsymbol{s}_{\text{direct}}$ and the corresponding regression coefficients using the direct approach, the solution can be expressed using a vector of weights $\boldsymbol{\zeta}$ (**Kitanidis1996b**; e.g., Miller et al., 2020):

$$\boldsymbol{s}_{\text{direct}} = \mathbf{X}\boldsymbol{\beta} + \mathbf{Q}\mathbf{H}^T\boldsymbol{\zeta}. \tag{S2}$$

There are two unknown vectors in Eq.S2, $\boldsymbol{\zeta}$ and $\boldsymbol{\beta}$. We solve for these vectors through a linear block system (e.g., Michalak et al., 2004; Miller et al., 2020):

$$\begin{bmatrix} \mathbf{HQH}^T + \mathbf{R} & \mathbf{HX} \\ (\mathbf{HX})^T & \mathbf{0} \end{bmatrix} \begin{bmatrix} \boldsymbol{\zeta} \\ \boldsymbol{\beta} \end{bmatrix} = \begin{bmatrix} \boldsymbol{z} \\ \mathbf{0} \end{bmatrix}, \tag{S3}$$

after computing for $\boldsymbol{\zeta}$ and $\boldsymbol{\beta}$, we can plug them back into Eq. S2 to solve for $\boldsymbol{s}_{\text{direct}}$.

This direct approach can yield physically unrealistic negative CH_4 fluxes (e.g., Miller, Michalak, & Levi, 2014), so we use the limited-memory Broyden–Fletcher–Goldfarb–Shanno algorithm with bound constraints (L-BFGS-B). This algorithm will minimize the cost function subject to the requirement that the estimated fluxes be non-negative ($\boldsymbol{s} \geq 0$) (e.g., R. H. Byrd et al., 1995; R. Byrd et al., 2003). In our study, we first solve for the unconstrained system using the direct approach (Eq. S3) to generate an initial flux estimate. Then, we use the L-BFGS-B to minimize the cost function and iteratively solve for the final non-negative flux estimate $\boldsymbol{s}$ (e.g., R. H. Byrd et al., 1995; R. Byrd et al., 2003). We choose L-BFGS-B for this step because it allows us to efficiently minimize the cost function without excessive memory requirements (R. H. Byrd et al., 1995; R. Byrd et al., 2003).

We also estimate posterior uncertainties as part of the inverse model, and more details of our approach are described by Michalak et al. (2004).

S0.2 Additional details on the BIC

A major challenge in interpreting the effects of multiple environmental drivers is the potential for collinearity. For example, when environmental drivers have similar spatial or temporal patterns, collinearity can make it difficult for the inverse model to distinguish their individual effects. To address this issue, we apply the Variance Inflation Factor (VIF) for each candidate combination of environmental drivers, which is an approach used by many existing studies (Marquardt, 1970). A VIF gives us information on whether an environmental driver is bringing unique information to the model, or whether it is mostly repeating information already provided by the other drivers. The equation that calculates the VIF can be described as:

$$\text{VIF}_i = \frac{1}{1 - R_i^2} \tag{S4}$$

where R_i^2 measures how well an environmental driver (x_i) can be explained by the other environmental drivers. R_i^2 has a range from 0 to 1, and a higher R_i^2 value means that the environmental driver is highly correlated with a linear combination of the other drivers. Consequently, a larger VIF indicates that the predictor is more correlated with the remaining predictors, and a VIF of 10 is a commonly used threshold to detect collinearity (e.g., Kutner, 2005). In our study, we filter out the models with a VIF larger than 10, and detailed information on VIF can be found in Marquardt (1970).

S0.3 Additional details on the calibration scales for CARVE and Arctic-CAP aircraft data

CARVE CH_4 data were calibrated to the WMO X2004 scale, and Arctic-CAP data were calibrated to the X2004A scale, which was implemented in July 2015 (https://gml.noaa.gov/ccl/ch4_scale.html). To investigate the impact of scale differences, we examined CARVE flask CH_4 data as a proxy for the insitu data, which is not as easily re-processed to the updated scale. We find that CARVE flask data on the X2004A scale are 0.3-0.6 ppb lower than flask data calibrated to the X2004 scale. Differences of this magnitude in the observational data would have a negligible impact on our results of growing season annual emissions. Note that the inversion is performed independently for each year, and all aircraft observations within a given inversion year are on the same calibration scale.

References

Arora, V. K., Melton, J. R., & Plummer, D. (2018). An assessment of natural methane fluxes simulated by the CLASS-CTEM model. *Biogeosciences*, *15*(15), 4683–4709. https://doi.org/10.5194/bg-15-4683-2018

Byrd, R. H., Lu, P., Nocedal, J., & Zhu, C. (1995). A limited memory algorithm for bound constrained optimization. *SIAM J. Sci. Comput.*, *16*(5), 1190–1208. https://doi.org/10.1137/0916069

Byrd, R., Lu, P., Nocedal, J., & Zhu, C. (2003). A limited memory algorithm for bound constrained optimization. *SIAM J. Sci. Comput.*, *16*. https://doi.org/10.1137/0916069

Clark, D. B., Mercado, L. M., Sitch, S., Jones, C. D., Gedney, N., Best, M. J., Pryor, M., Rooney, G. G., Essery, R. L. H., Blyth, E., Boucher, O., Harding, R. J., Huntingford, C., & Cox, P. M. (2011). The Joint UK Land Environment Simulator (JULES), model description – Part 2: Carbon fluxes and vegetation dynamics. *Geosci. Model Dev.*, *4*(3), 701–722. https://doi.org/10.5194/gmd-4-701-2011

Gourdji, S. M., Mueller, K. L., Yadav, V., Huntzinger, D. N., Andrews, A. E., Trudeau, M., Petron, G., Nehrkorn, T., Eluszkiewicz, J., Henderson, J., Wen, D., Lin, J., Fischer, M., Sweeney, C., & Michalak, A. M. (2012). North American CO_2 exchange: Inter-comparison of modeled estimates with results from a fine-scale atmospheric inversion. *Biogeosciences*, *9*(1), 457–475. https://doi.org/10.5194/bg-9-457-2012

Hodson, E. L., Poulter, B., Zimmermann, N. E., Prigent, C., & Kaplan, J. O. (2011). The El Niño–Southern Oscillation and wetland methane interannual variability. *Geophys. Res. Lett.*, *38*(8). https://doi.org/10.1029/2011GL046861

Ito, A., & Inatomi, M. (2012). Use of a process-based model for assessing the methane budgets of global terrestrial ecosystems and evaluation of uncertainty. *Biogeosciences*, *9*(2), 759–773.

Kitanidis, P. K., & Lane, R. W. (1985). Maximum likelihood parameter estimation of hydrologic spatial processes by the Gauss-Newton method. *J. Hydrol.*, *79*(1), 53–71. https://doi.org/10.1016/0022-1694(85)90181-7

Kitanidis, P. K., & Vomvoris, E. G. (1983). A geostatistical approach to the inverse problem in groundwater modeling (steady state) and one-dimensional simulations. *Water Resour. Res.*, *19*(3), 677–690. https://doi.org/10.1029/WR019i003p00677

Kleinen, T., Brovkin, V., & Schuldt, R. J. (2012). A dynamic model of wetland extent and peat accumulation: results for the Holocene. *Biogeosciences*, *9*(1), 235–248. https://doi.org/10.5194/bg-9-235-2012

Kleinen, T., Mikolajewicz, U., & Brovkin, V. (2020). Terrestrial methane emissions from the Last Glacial Maximum to the preindustrial period. *Clim. Past*, *16*(2), 575–595. https://doi.org/10.5194/cp-16-575-2020

Kutner, M. (2005). *Applied linear statistical models*. McGraw-Hill Irwin. https://books.google.com/books?id=0xqCAAAACAAJ

Li, T., Huang, Y., Zhang, W., & Song, C. (2010). CH_4MODwetland: A biogeophysical model for simulating methane emissions from natural wetlands. *Ecol. Model.*, *221*(4), 666–680. https://doi.org/10.1016/j.ecolmodel.2009.05.017

Liu, L., Zhuang, Q., Oh, Y., Shurpali, N. J., Kim, S., & Poulter, B. (2020). Uncertainty quantification of global net methane emissions from terrestrial ecosystems using a mechanistically based biogeochemistry model [e2019JG005428 2019JG005428]. *J. Geophys. Res.-Biogeo.*, *125*(6), e2019JG005428. https://doi.org/10.1029/2019JG005428

Marquardt, D. W. (1970). Generalized inverses, ridge regression, biased linear estimation, and nonlinear estimation. *Technometrics*, *12*(3), 591–612. https://doi.org/10.2307/1267205

McGuire, A. D., Christensen, T. R., Hayes, D., Heroult, A., Euskirchen, E., Kimball, J. S., Koven, C., Lafleur, P., Miller, P. A., Oechel, W., Peylin, P., Williams, M., & Yi, Y. (2012). An assessment of the carbon balance of arctic tundra: Comparisons among observations, process models, and atmospheric inversions. *Biogeosciences*, *9*(8), 3185–3204. https://doi.org/10.5194/bg-9-3185-2012

Michalak, A. M., Bruhwiler, L., & Tans, P. P. (2004). A geostatistical approach to surface flux estimation of atmospheric trace gases. *J. Geophys. Res.-Atmos.*, *109*(D14). https://doi.org/10.1029/2003JD004422

Miller, S. M., Michalak, A. M., & Levi, P. J. (2014). Atmospheric inverse modeling with known physical bounds: An example from trace gas emissions. *Geosci. Model Dev.*, *7*(1), 303–315. https://doi.org/10.5194/gmd-7-303-2014

Miller, S. M., Saibaba, A. K., Trudeau, M. E., Mountain, M. E., & Andrews, A. E. (2020). Geostatistical inverse modeling with very large datasets: An example from the Orbiting Carbon Observatory 2 (OCO-2) satellite. *Geosci. Model Dev.*, *13*(3), 1771–1785. https://doi.org/10.5194/gmd-13-1771-2020

Miller, S. M., Miller, C. E., Commane, R., Chang, R. Y.-W., Dinardo, S. J., Henderson, J. M., Karion, A., Lindaas, J., Melton, J. R., Miller, J. B., Sweeney, C., Wofsy, S. C., & Michalak, A. M. (2016). A multiyear estimate of methane fluxes in Alaska from CARVE atmospheric observations. *Global Biogeochem. Cy.*, *30*(10), 1441–1453. https://doi.org/10.1002/2016GB005419

Miller, S. M., Worthy, D. E. J., Michalak, A. M., Wofsy, S. C., Kort, E. A., Havice, T. C., Andrews, A. E., Dlugokencky, E. J., Kaplan, J. O., Levi, P. J., Tian, H., & Zhang, B. (2014). Observational constraints on the distribution, seasonality, and environmental predictors of North American boreal methane emissions. *Global Biogeochem. Cy.*, *28*(2), 146–160. https://doi.org/10.1002/2013GB004580

Riley, W. J., Subin, Z. M., Lawrence, D. M., Swenson, S. C., Torn, M. S., Meng, L., Mahowald, N. M., & Hess, P. (2011). Barriers to predicting changes in global terrestrial methane fluxes: Analyses using CLM4Me, a methane biogeochemistry model integrated in CESM. *Biogeosciences*, *8*(7), 1925–1953. https://doi.org/10.5194/bg-8-1925-2011

Ringeval, B., de Noblet-Ducoudré, N., Ciais, P., Bousquet, P., Prigent, C., Papa, F., & Rossow, W. B. (2010). An attempt to quantify the impact of changes in wetland extent on methane emissions on the seasonal and interannual time scales. *Global Biogeochem. Cy.*, *24*(2). https://doi.org/10.1029/2008GB003354

Shu, S., Jain, A. K., & Kheshgi, H. S. (2020). Investigating wetland and nonwetland soil methane emissions and sinks across the contiguous United States using a land surface model [e2019GB006251 2019GB006251]. *Global Biogeochem. Cy.*, *34*(7), e2019GB006251. https://doi.org/10.1029/2019GB006251

Singarayer, J. S., Valdes, P. J., Friedlingstein, P., Nelson, S., & Beerling, D. J. (2011). Late holocene methane rise caused by orbitally controlled increase in tropical sources. *Nature*, *470*(7332), 82–85. https://doi.org/10.1038/nature09739

Spahni, R., Wania, R., Neef, L., van Weele, M., Pison, I., Bousquet, P., Frankenberg, C., Foster, P. N., Joos, F., Prentice, I. C., & van Velthoven, P. (2011). Constraining global methane emissions and uptake by ecosystems. *Biogeosciences*, *8*(6), 1643–1665. https://doi.org/10.5194/bg-8-1643-2011

Tian, H., Xu, X., Liu, M., Ren, W., Zhang, C., Chen, G., & Lu, C. (2010a). Spatial and temporal patterns of CH_4 and N_2O fluxes in terrestrial ecosystems of North America during 1979–2008: Application of a global biogeochemistry model. *Biogeosciences*, *7*(9), 2673–2694. https://doi.org/10.5194/bg-7-2673-2010

Tian, H., Xu, X., Liu, M., Ren, W., Zhang, C., Chen, G., & Lu, C. (2010b). Spatial and temporal patterns of CH_4 and N_2O fluxes in terrestrial ecosystems of North America during 1979–2008: application of a global biogeochemistry model. *Biogeosciences*, *7*(9), 2673–2694. https://doi.org/10.5194/bg-7-2673-2010

Wania, R., Ross, I., & Prentice, I. C. (2010a). Implementation and evaluation of a new methane model within a dynamic global vegetation model: Lpj-whyme v1.3.1. *Geosci. Model Dev.*, *3*(2), 565–584. https://doi.org/10.5194/gmd-3-565-2010

Wania, R., Ross, I., & Prentice, I. C. (2010b). Implementation and evaluation of a new methane model within a dynamic global vegetation model: LPJ-WHyMe v1.3.1. *Geosci. Model Dev.*, *3*(2), 565–584. https://doi.org/10.5194/gmd-3-565-2010

Westermann, S., Barboux, C., Bartsch, A., Delaloye, R., Grosse, G., Heim, B., Hugelius, G., Irrgang, A., Kääb, A. M., Matthes, H., Nitze, I., Pellet, C., Seifert, F. M., Strozzi, T., Wegmüller, U., Wieczorek, M., & Wiesmann, A. (2024). ESA permafrost climate change initiative (Permafrost_cci): Permafrost extent for the Northern Hemisphere, v4.0. https://doi.org/10.5285/93444bc1c4364a59869e004bf9bfd94a

Zhang, Z., Zimmermann, N. E., Kaplan, J. O., & Poulter, B. (2016). Modeling spatiotemporal dynamics of global wetlands: comprehensive evaluation of a new sub-grid TOPMODEL parameterization and uncertainties. *Biogeosciences*, *13*(5), 1387–1408. https://doi.org/10.5194/bg-13-1387-2016

Zhu, Q., Liu, J., Peng, C., Chen, H., Fang, X., Jiang, H., Yang, G., Zhu, D., Wang, W., & Zhou, X. (2014). Modelling methane emissions from natural wetlands by development and application of the TRIPLEX-GHG model. *Geosci. Model Dev.*, *7*(3), 981–999.

Zhu, Q., Riley, W. J., Tang, J., Collier, N., Hoffman, F. M., Yang, X., & Bisht, G. (2019). Representing nitrogen, phosphorus, and carbon interactions in the E3SM land model: Development and global benchmarking. *J. Adv. Model. Earth Sy.*, *11*(7), 2238–2258. https://doi.org/10.1029/2018MS001571